The Journal of Experimental Biology 213, 2038-2047

doi:10.1242/jeb.040162

Numerical simulation of a pectoral fin during labriform swimming

Kourosh Shoele and Qiang Zhu*

Department of Structural Engineering, University of California, San Diego, La Jolla, CA 92093, USA

*Author for correspondence (qizhu@ucsd.edu)

Accepted 21 February 2010

SUMMARY

We numerically examine the fluid–structure interaction and force generation of a skeleton-reinforced fin that geometrically, structurally and kinematically resembles the pectoral fin of a fish during labriform swimming. This fin contains a soft membrane with negligible bending stiffness and 12 embedded rays (modeled as beams). A potential flow-based boundary element model is applied to solve the fluid flow around the fin, in which the vorticity field is modeled as thin vorticity sheets shed from prescribed locations (the sharp trailing edge). The fin motion is actuated by dorsoventral and anteroposterior rotations of the rays (the motion of each ray is controlled individually), as well as pitching motion of the baseline. Consequently, the fin undergoes a combination of flapping (lift-based) and rowing (drag-based) motions typical in labriform swimming. The fin motion contains two strokes: a recovery stroke and a power stroke. The performance of the fin depends upon kinematic parameters such as the Strouhal number, the phase lag between rays, the pitching motion of the baseline and the passive deformations of the rays. The most interesting finding is that the strengthening of the ray at the leading edge plays a pivotal role in performance enhancement by reducing the effective angle of attack and decreasing the power expenditure during the recovery stroke.

Supplementary material available online at http://jeb.biologists.org/cgi/content/full/213/12/2038/DC1

Key words: fluid-structure interaction, skeleton-reinforced membrane, pectoral fin, labriform locomotion.

INTRODUCTION

Fishes rely upon different fluid–structure interaction mechanisms for locomotion. To date, about 20 locomotion modes have been identified in steady swimming (Webb, 1994). This diversity comes from different combinations of undulation of flexible bodies and unsteady flapping of body-attached fins.

Morphologically, fish fins fall into two categories: median fins (e.g. dorsal fins, ventral fins and caudal fins) and paired fins (e.g. pectoral fins and pelvic fins). Paired fins are employed mostly in motion stabilization, maneuvering and braking, as well as labriform swimming (Webb, 1973; Blake, 1979; Vogel, 1994; Standen, 2008). Indeed, in many species (e.g. teleosts), pectoral fins are often the primary locomotion devices (Videler, 1993).

Fish fins are highly mobile, collapsible and capable of changing their effective areas. A pectoral fin consists of a pectoral girdle skeleton, an arrow of four radials that forms a basal support for the fin, a fibrocartilage pad upon which the rays can rotate, a series of fin rays with rotational bases, and muscles that enable movements of the fin rays. Structurally, it forms a skeleton-reinforced membrane system – a soft (and thin) collagenous membrane strengthened by bony fin rays. The Young's modulus (E) of the fin rays is much larger than that of the membrane so that the bending stiffness of the fin is much higher in the direction of the embedded rays compared with those in other directions (Lauder et al., 2006; Lauder and Madden, 2007). The non-uniform distribution of these rays imparts anisotropic structural flexibility such that certain deformations may be more easily attainable while others are restricted. In many fishes, the first two rays near the leading edge strongly bond together along their length through connective tissues to form a strengthened leading edge (Videler, 1993). This characteristic will later be shown to have an important effect upon the propulsive performance of the fin.

The ray fin architecture enables multi-degree-of-freedom control over the motion and deformation of the fins. The basal end of each ray attaches to four separate muscles so that its rotational motion can be actuated individually (i.e. independent of the motions of other rays). In addition, through embedded tendons and a bi-laminar structure of each ray, the fish can actively change the curvature along a ray. According to morphological studies (Harder, 1975; Kardong, 1998), a fin ray contains a central bundle of collagen surrounded by small segmented bony elements called hemitrichs. These elements are paired and resemble a bimetallic strip with two elongated bony elements separated by the central collagen core. A hemitrich is connected with short ligaments and elastic fibers. Through such structures, bending moments can be created along the length of a ray.

Kinematically, among fishes capable of sustained pectoral fin propulsion in high speeds, labriform swimming is a combination of an up-and-down (dorsoventral) flapping motion, a back-and-forth (anteroposterior) rowing motion, as well as a pitching motion of the baseline formed by the basal ends of the rays (e.g. Drucker et al., 2006). Although, in certain cases, a fish may perform pure flapping motion (which is also called 'lift-based' swimming) or pure rowing motion ('drag-based' swimming) (Blake, 1983; Vogel, 1994), in general fish rarely exhibit pure rowing or flapping movements. Instead, in most cases, a combination of them is applied. Owing to the highly flexible membrane and the fin rays, as well as the hydrodynamic interactions of the fins with the surrounding water, pectoral fin motions are usually complicated (Gibb et al., 1994; Lauder and Jayne, 1996).

The propulsion performance of pectoral fins is affected by various factors, including, for example, the geometry of the fin, the length and flexibility of the embedded rays, as well as the amplitude, orientation and phase of each ray during locomotion. In some fishes (e.g. trout), the baseline of the fin undergoes significant pitching

motion, which may affect the capacity of force generation. For example, in rainbow trout, the baseline of the pectoral fin is connected with the body through a flexible hinge joint that allows rotational motion (Drucker and Lauder, 2003).

In the present study, we numerically model the effects of structural and kinematic parameters upon the performance of an idealized pectoral fin in labriform swimming. In particular, we concentrate upon the effects of the frequency of motion, the baseline rotation, the phase lag between the rays, and the bending stiffness of the rays. For this purpose, we will solve the involved fluid–structure interaction problem with a fully coupled model. Special effort is expended on clarifying the possible performance-enhancing effects of strengthened leading edge and the rotation of the baseline. Compared with our previous studies of caudal fin dynamics (Zhu and Shoele, 2008) and pectoral fin dynamics in pure lift-based locomotion (Shoele and Zhu, 2009), our current work possesses the following characteristics: (1) instead of simple mediolateral motions (Zhu and Shoele, 2008) or dorsoventral motions (Shoele and Zhu, 2009), herein we consider a much more complicated and realistic fin kinematics including anteroposterior, dorsoventral and baseline pitching motions enabled by synchronized ray rotations and reorientation of the baseline; (2) we consider a more realistic fin flexibility in which the rays have different stiffness; and (3) the hydrodynamic effects of both the phase lag between rays and the baseline pitching motion are explored.

The rest of the paper is organized as follows. In the next section we define the geometry, structure and kinematics of the simplified pectoral fin. This is followed by a brief description of the fluid–structure interaction formulation as well as the numerical approach. Numerical results, including the force generation and propulsion efficiency of the fin, and the corresponding flow fields, are then provided. Based upon these results, conclusions are drawn.

MATERIALS AND METHODS

Geometry and internal structure of the idealized fin

The geometry and kinematics of the fin are described within a Cartesian coordinate system (x, y, z), where x corresponds to the posterior direction, z is along the dorsoventral axis and y is along the mediolateral axis. At its initial configuration, the fin lies within the x–z plane.

Pectoral fin shape varies among species as a consequence of different habitats and different roles in swimming. Instead of exactly duplicating the geometry and kinematics of the fin of a specific species (Mittal et al., 2006; Bozkurttas et al., 2009), in the current investigation we consider an idealized fin with simplified geometry, internal structure and kinematics. Specifically, we use a trapezoidal shaped fin with small base and long leading edge to imitate pectoral fins of many species (e.g. *Stethojulis trilineata*, *Abudefuf saxatilis*). From the biomimetic point of view, simplified designs are also easier to be manufactured.

As shown in Fig. 1, we consider a trapezoidal shaped pectoral fin whose geometry and structural response are determined by twelve embedded rays, Ray 1 to Ray 12. The leading ends of these rays are distributed evenly along a straight baseline, which in its initial position forms an angle of θ_b with the $-x$-axis. The angle between these rays and the x-axis, α_{i0}, varies evenly between $90\,\text{deg}-\theta_b$ at Ray 1 and $45\,\text{deg}-\theta_b$ at Ray 12. The length of Ray 1 is L, and the length of Ray 12 is $0.3L$. The baseline length is chosen to be $0.3L$. The lengths of other rays are chosen so that their trailing ends also form a straight line, the trailing edge. The thickness d of the fin is $0.02L$.

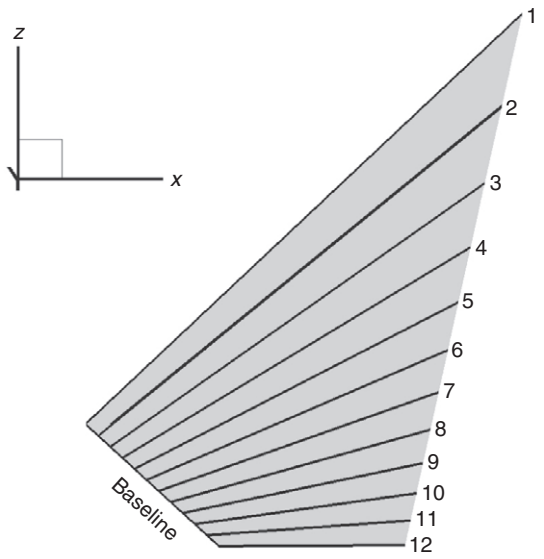

Fig. 1. Geometry and structure of a simplified pectoral fin.

The structural property of a single ray is characterized by its bending stiffness, EI; in our simulations we consider a normalized bending stiffness $EI'=EI/\rho U^2L^4$, where ρ is the density of the fluid and U is the speed of the forward motion. For perspective about the possible range of EI', we note that according to the argument by Alben et al. (Alben et al., 2007), during normal swimming the bending energy stored in the fin must be balanced by the kinetic energy of the flow, leading to an estimate that $EI\sim\rho U^2L^4/12$.

We assume that the material surrounding the rays behaves like a membrane that can withstand stretching but not bending. This assumption is justified by the fact that this membrane is very thin and its Young's modulus is much smaller than that of the rays (Lauder et al., 2006). Correspondingly, the membrane is physically modeled as distributions of linear springs between neighboring rays, which introduce a constraint upon the area change of the fin.

For generality, in the following simulations we consider a dimensionless problem in which all the properties are normalized by ρ, U and L.

Kinematics

The flapping/rowing motions of the fin are actuated by rotations of the embedded rays. During the locomotion the i-th ray undergoes two rotations simultaneously: a rotation $\varphi_i(t)$ around the x-axis (the dorsoventral motion), and a variation of the angle $\alpha_i(t)$ between this ray and the x-axis (the anteroposterior motion) (Fig. 2).

Following experimental observations of labriform swimming (e.g. Drucker et al., 2006), each locomotion period T is separated into two sub-periods, a recovery stroke (abduction) with duration T_r and a power stroke (adduction) with duration T_p; based on observations we choose $T_r=T_p=T/2$. During the recovery stroke $0\le t\le T_r$, the baseline rotates (with respect to its center) around the y axis from its initial position to the horizontal position (i.e. baseline pitching motion). Meanwhile all the rays have anterior rotations so that the angle between them and the x-axis varies as $\alpha_i(t)=\alpha_{i0}+(\alpha_0/2)[1-\cos(\pi t/T_r)]$. In our simulations we relate α_0 with

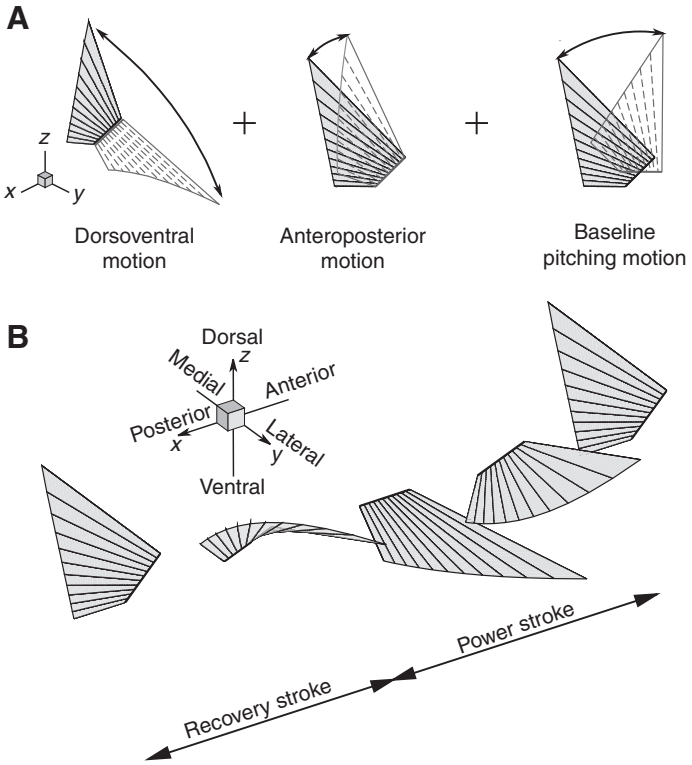

Fig. 2. Kinematics of fin motion: (A) different components of fin kinematics, (B) 3-D view of the fin motion during recovery and power strokes.

θ_b through $\alpha_0=\theta_b+45$ deg. With this restriction the angle formed by the leading edge and the *x*-axis always reaches 135 deg at the end of the recovery stroke.

Together with the baseline rotation and the anterior rotations of the rays, each ray also undergoes dorsoventral rotations around the *x*-axis to achieve the flapping motion. The rotational angle of the *i*-th ray is depicted as:

$$\phi_i(t)=\begin{cases}0, & (\pi+\psi_i)t/T_r<\psi_i\\ \dfrac{\phi_0}{2}\left\{1-\cos\left[\dfrac{(\pi+\psi_i)t}{T_r}-\psi_i\right]\right\}, & (\pi+\psi_i)t/T_r>\psi_i\end{cases}, \quad (1)$$

where ψ_i is the phase lag of the flapping motion of the *i*-th ray, which varies linearly from 0 at Ray 1 to ψ_{12} at Ray 12. The parameter ϕ_0, corresponding to the maximum rotation angle, is chosen to be 135 deg (unless otherwise specified).

During the power stroke $T_r<t\leq T$, the baseline rotates back to its original position. The rays rotate back towards the posterior direction, which is mathematically described as $\alpha_i(t)=\alpha_{i0}+(\alpha_0/2)[1-\cos(\pi t/T_r)]$. The flapping motion becomes:

$$\phi_i(t)=\begin{cases}\phi_0, & (\pi+\psi_i)(t-T_r)/T_p<\psi_i\\ \dfrac{\phi_0}{2}\left\{1+\cos\left[\dfrac{(\pi+\psi_i)(t-T_r)}{T_p}-\psi_i\right]\right\}, & (\pi+\psi_i)(t-T_r)/T_p>\psi_i\end{cases}. \quad (2)$$

As a measure of the frequency of motion, we define a Strouhal number, *St*, based upon the length of the leading edge *L*, the forward speed *U*, and the period *T*, i.e. $St=L/UT$.

See Movies 1–3 in supplementary material, which show the fin kinematics during a recovery-power cycle.

Mathematical formulations and numerical methods

A fluid–structure interaction model is developed to study the dynamics of the aforementioned ray fin. This model, *per se*, contains three inter-coupled models: the rays are modeled as Euler–Bernoulli beams that can sustain bending and stretching loads; the membrane between neighboring rays is represented by distributions of linear springs; and the flow field around the fin is assumed to be potential and mathematically described by using the boundary-integral equations. The fluid and structural models are numerically coupled through an iteration algorithm. The formulations and numerical issues of these models are briefly summarized below. Detailed descriptions can be found in Zhu and Shoele (Zhu and Shoele, 2008).

First, we model each ray as an axisymmetric beam with uniformly distributed bending stiffness, *EI*. For simplicity, the anisotropic properties of the ray, the tapering and branching near the trailing edge, as well as the active controlling mechanisms, are not considered in the current model [see for example Alben et al. (Alben et al., 2007) for a model of the active ray curvature control]. Physically, these rays are described as Euler–Bernoulli beams. Numerically, we use a three-dimensional nonlinear model to simulate their dynamic responses. First developed by Tjavajas et al. (Tjavajas et al., 1998), this method achieves fully nonlinear dynamic simulation of beams and cables that can be stretched, bent and twisted. Towards this end, we implement a dual Euler–Lagrangian coordinate system, including a global Euler coordinate system and a local Lagrangian coordinate system. A special treatment in this method is the employment of Euler parameters, instead of the conventional Euler angles, to achieve

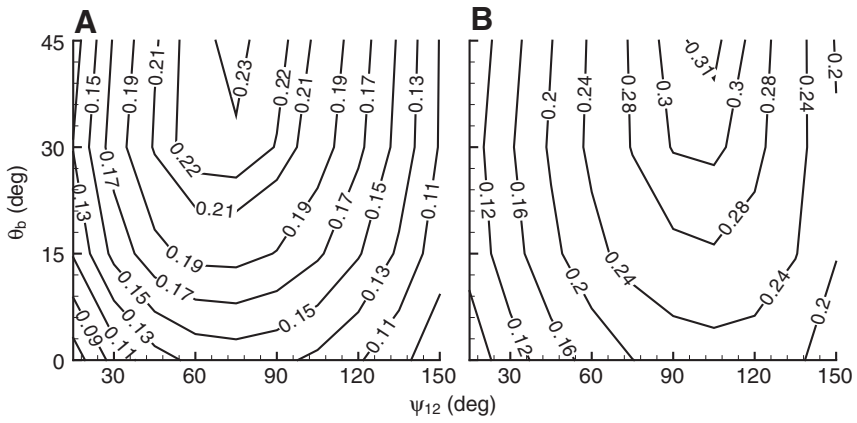

Fig. 3. Effects of the baseline pitching angle θ_b and the phase lag Ψ_{12} upon (A) the mean thrust coefficient $\bar{C}_T$ and (B) the propulsion efficiency η. The rays are rigid. St=0.4.

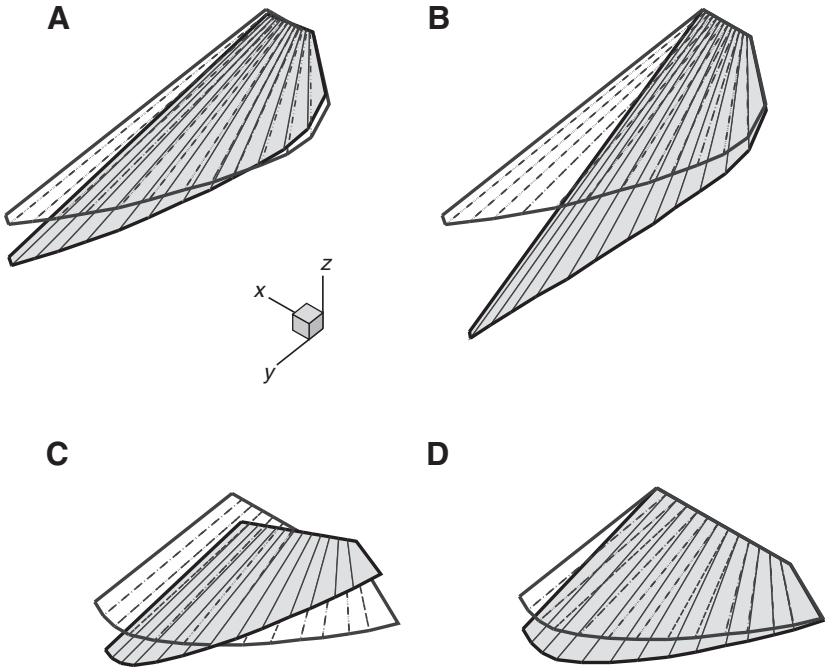

Fig. 4. The effectiveness of baseline rotation and phase lag between rays in changing the angle of attack of fins of high and low aspect ratios: (A) a high aspect ratio fin with baseline rotation, (B) a high aspect ratio fin with phase lag between rays, (C) a low aspect ratio fin with baseline rotation and (D) a low aspect ratio fin with phase lag between rays.

rotational transformations between the two coordinate systems. This method avoids the well-known singularity associated with Euler angles and is thus particularly suitable for simulations of arbitrary large motions of cables or beams. To model the viscoelastic behavior of the rays, we further replace E by $E[1+\nu(\partial/\partial t)]$, where the coefficient ν is chosen to be $0.2\,L/U$.

The membrane between neighboring rays is modeled as a distribution of linear springs that introduces a constraint upon the area change of the fin. As reported by Lauder et al. (Lauder et al., 2006), the membrane between fin rays has a Young's modulus of about 0.3–1.0 MPa. We further assume that the thickness of the membrane is $O(10^{-3})L$, the forward speed is $O(5)L$, and $L\sim(10^{-2})$ m. The stretching stiffness of the membrane per unit length is estimated to be $O(10)\rho U^2$; in the following simulations we choose it to be $25\rho U^2$.

In cases with high Reynolds numbers, the fluid viscosity is neglected so that the vector field representing the flow velocity can be conveniently described by using a spatial distribution of a scalar, the flow potential Φ. Vortex shedding occurs at the trailing edge. In the wake, the vorticity is distributed on an infinitely thin sheet (mathematically, a vorticity sheet is equivalent to a sheet of distributed dipoles). The strength of newly shed vorticity is evaluated using the Kutta condition so that no singularity exists at the trailing edge. Without any dissipation effect, the strength of the vorticity sheet remains unchanged once it leaves the trailing edge.

An iterative algorithm is implemented so that the fluid dynamics problem and the structural responses are solved separately within an iteration loop. To guarantee numerical stability of the structural solver, a small time step is required, while a much larger time step is used in the fluid solver to increase the speed of simulation. For this purpose, in our simulation, a single iteration loop involves one time step Δt in fluid dynamics calculation, and 50 time steps in structural simulation.

After the flow potential Φ is numerically determined, we calculate the hydrodynamic force $\mathbf{F}$ upon the fin by integrating the pressure p over its surface so that:

$$\mathbf{F}(t) = \iint_{S_b} p(\mathbf{x}',t)\,\mathbf{n}\,d\mathbf{x}' \,, \tag{3}$$

where $\mathbf{n}$ is a unit normal vector pointing into the fin surface and S_b is the surface of the fin. Using Bernoulli's equation, the pressure is determined as:

$$p(\boldsymbol{x},t) = -\rho\left\{\frac{\partial\Phi(\boldsymbol{x},t)}{\partial t} + \frac{1}{2}\left|\nabla\Phi(\boldsymbol{x},t)\right|^2\right\} . \tag{4}$$

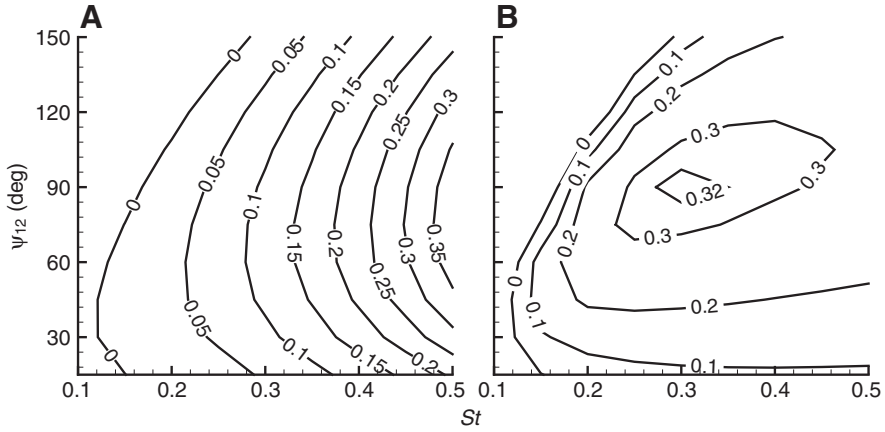

Fig. 5. (A) Mean thrust coefficient, $\bar{C}_T$, and (B) propulsion efficiency, η, as functions of the Strouhal number, St, and phase lag Ψ_{12}. The rays are rigid.

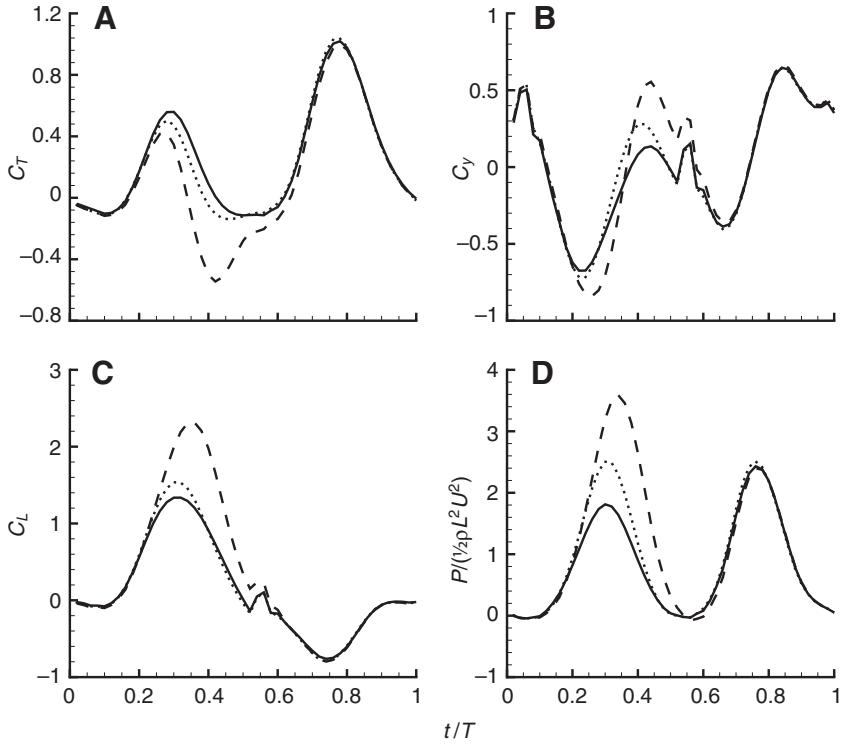

Fig. 6. Variations of (A) thrust coefficient (C_T), (B) lateral force coefficient (C_y), (C) lift coefficient (C_L) and (D) energy expenditure over one period for the fin with rigid rays (dotted lines), fin A (dashed lines) and fin B (solid lines). St=0.4, Ψ_{12}=60 deg, for the flexible fins EI'=0.5.

The power expenditure P is given as:

$$P(t) = -\iint_{S_b} p(\boldsymbol{x}',t)\boldsymbol{n}\cdot\boldsymbol{V}_b(\boldsymbol{x}',t)\,d\boldsymbol{x}' \ , \quad (5)$$

where $\mathbf{V}_b$ represents velocity of the body.

The performance of the fin is characterized by its ability to generate thrust force F_T (the component of $\mathbf{F}$ in the $-x$ direction), lift force F_L (the component of $\mathbf{F}$ in the z direction) and lateral force F_y (the component of $\mathbf{F}$ in the y direction). Correspondingly, we define a thrust coefficient $C_T=F_T/\frac{1}{2}\rho U^2L^2$, a lift coefficient $C_L=F_L/\frac{1}{2}\rho U^2L^2$, and a lateral force coefficient $C_y=F_y/\frac{1}{2}\rho U^2L^2$. Another important index is the propulsion efficiency η, defined as $\eta=\bar{F}_T\times U/\bar{P}$, where $\bar{F}_T$ and $\bar{P}$ represent the thrust force and power consumption averaged over one period T, respectively.

RESULTS

Effects of kinematic parameters

Based upon experimental observations, it has been suggested that variations of baseline angle might be an important factor determining the propulsive performance of pectoral fins (Lauder and Jayne, 1996; Walker and Westneat, 2002a). As mentioned by Walker (Walker, 2004), there are two mechanisms to achieve the pitching motion (i.e. the variation of the angle of attack) of the

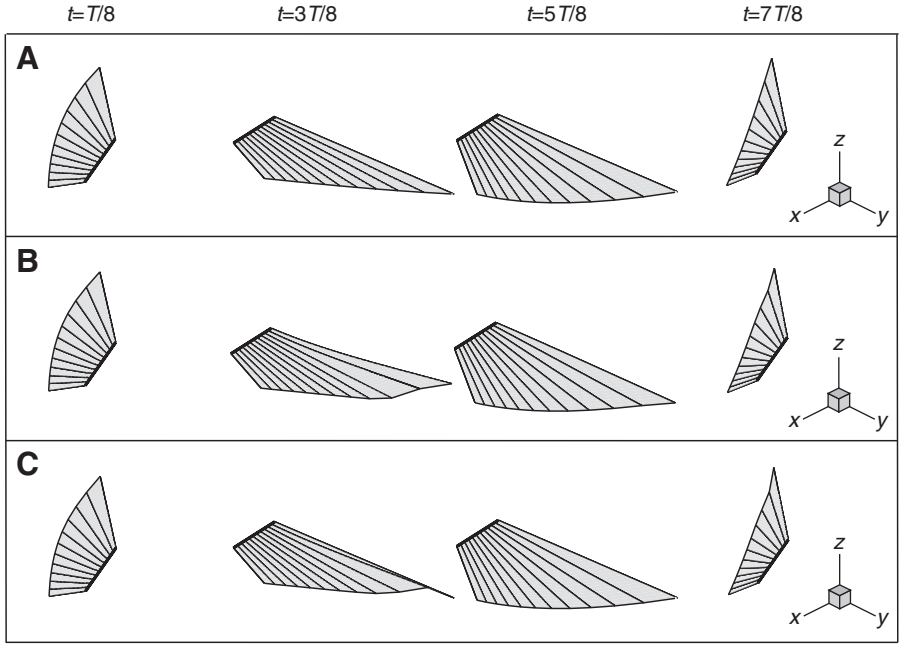

Fig. 7. The motion and deformation of (A) the fin with rigid rays, (B) fin A and (C) fin B. St=0.4, Ψ_{12}=60 deg, for the flexible fins EI'=0.5.

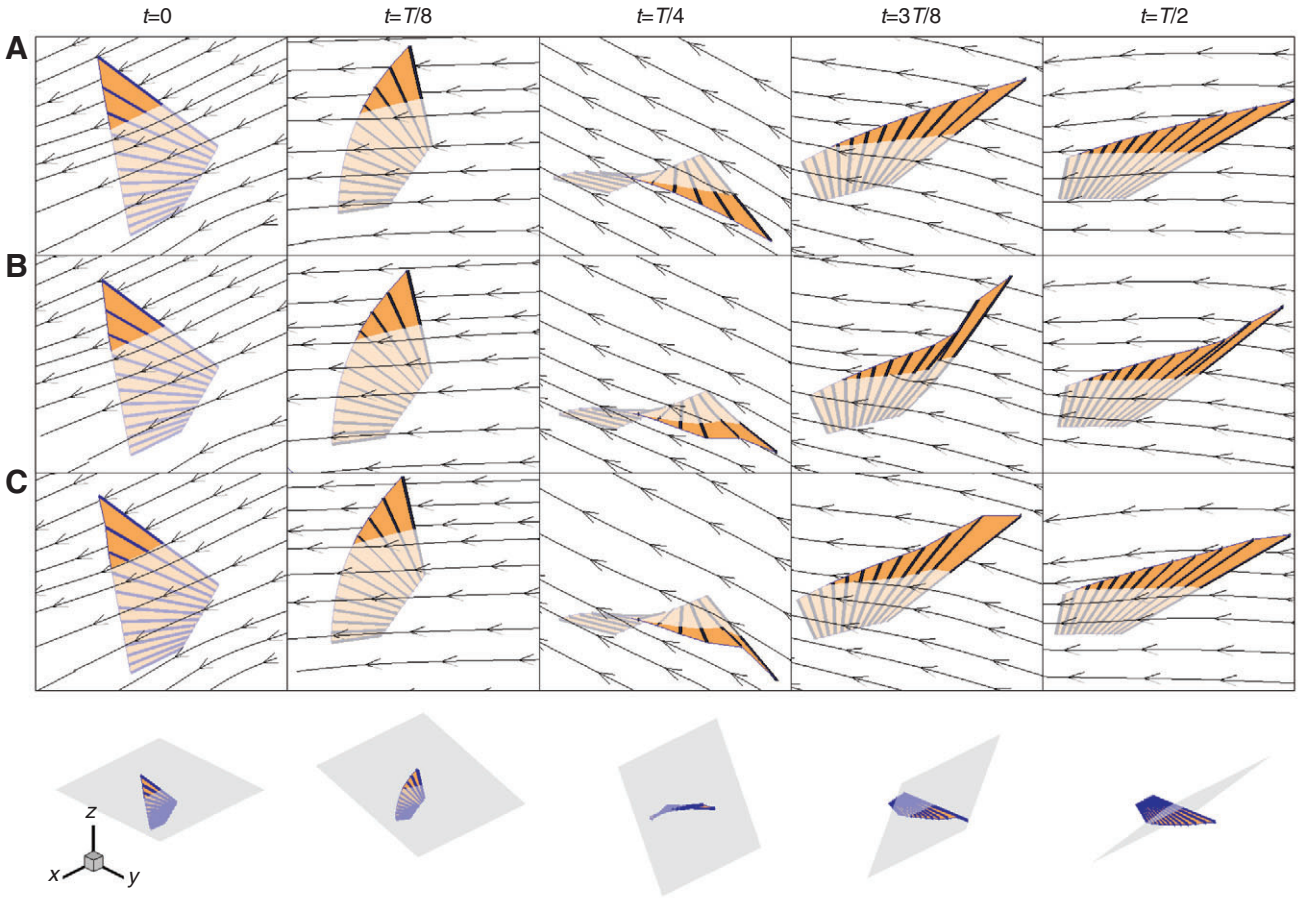

Fig. 8. Shape variation of the fin and the in-plane streamlines within a plane rotating with the flapping motion of the fin during the recovery stroke. The streamlines are plotted in a reference system that follows the translational motion of the center point of Ray 1. The three cases are: (A) the fin with rigid rays, (B) fin A and (C) fin B. St=0.4, Ψ_{12}=60 deg, for the flexible fins EI'=0.5.

fin. The first one is by controlling the phase differences between leading and trailing fin rays. This is the primary method in fishes lacking shoulder plate mobility. Through this method, a fish is able to create a large spanwise variation in the angle of attack. By doing this it is possible to achieve optimal pitching motion along the fin. The second mechanism is by reorientation of the fin root (the baseline). It is observed that in certain species, due to the existence of joints in shoulder plates, large baseline rotations are allowed. For instance, Drucker and Lauder (Drucker and Lauder, 2003) observed that trout are able to change their fin baseline angle by over 30 deg. Similar behavior has been reported in boxfish (Blake, 1977). The advantage of baseline rotation is to achieve a relatively large angle between the fin and the incoming flow in the adduction (power) phase, which in turn produces larger thrust force. These two mechanisms of fin rotation can be combined, e.g. using phase difference between rays for drag reduction in the abduction phase to reduce power expenditure and using a combination of baseline rotation and phase lag along fin span in the adduction phase to increase thrust force.

In order to illustrate the effects of baseline rotation and the phase lag between fin rays, we herein study the dynamic performance of a fin with rigid rays within a range of baseline pitching angle 0 deg≤θ_b≤45 deg (where θ_b=0 deg corresponds to the case with no baseline rotation) and the phase lag 15 deg≤Ψ_{12}≤150 deg. In Fig. 3 we plot the mean thrust coefficient $\overline{C}_T$, the mean lateral force coefficient $\overline{C}_y$, the mean lift force coefficient $\overline{C}_L$ and the propulsion efficiency η at St=0.4. It is observed that the baseline rotation can significantly increase both $\overline{C}_T$ and η.

A possible factor that determines the effectiveness of phase lag between rays and baseline rotation is the geometry of the fin. According to Walker and Westneat (Walker and Westneat, 2002b), one of the important differences between rowing and flapping pectoral fins is their aspect ratios. This parameter also affects the relative importance of baseline rotation and phase lag in the fin feathering motion. For example, for pectoral fins with large aspect ratios (slender fins), variations of the fin shape near the tip are determined mostly by the phase lag (Fig. 4A,B). This demonstrates why species, such as bird wrasse (*Gomphosus varius*), with relatively large aspect ratio use mostly phase lag between rays to change the angle of attack of the fin (Walker and Westneat, 1997). For pectoral fins with lower aspect ratios, e.g. in the threespine stickleback (*Gasterosteus aculeatus*), the baseline rotation is more effective (Walker, 2004) (Fig. 4C,D). It is worth pointing out that, besides fin aspect ratio, there are other parameters that affect fin performance, such as fin shape, active geometry changes (Lauder and Jayne, 1996) and moments of fin area.

In the following simulations, we specify θ_b to be 45 deg.

Fig. 5 shows the variation of the mean thrust coefficient and the propulsion efficiency over 0.1≤St≤0.5 and 15 deg≤Ψ_{12}≤150 deg for the fin with rigid rays. In terms of the propulsion efficiency, optimal performance (around 0.32) is achieved near St~0.4 and Ψ_{12}~90 deg.

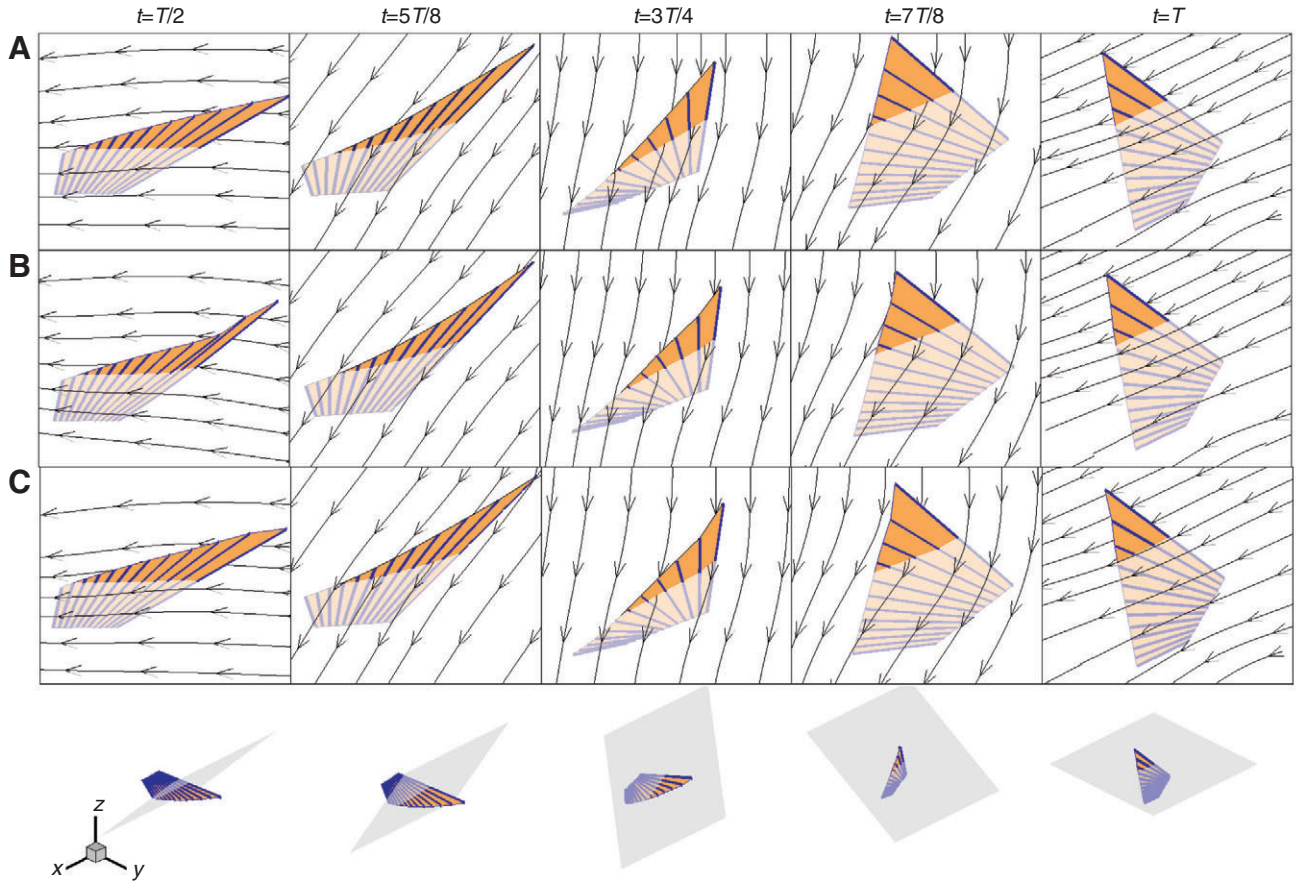

Fig. 9. Shape variation of the fin and the in-plane streamlines within a plane rotating with the flapping motion of the fin during the power stroke. The parameters are the same as those in Fig. 8.

Effects of structural flexibility

In order to study the effects of structural flexibility upon the performance of the fin, we examine the capacity of force generation by two slightly different flexible fins; in one of them (hereafter referred to as fin A) the mechanical properties of all the rays are identical, while in the second one (fin B) the ray at the leading edge (Ray 1) is strengthened so that its effective diameter is twice as large as other rays (i.e. the bending stiffness of the first ray is 15 times larger than that of other rays). The configuration of the second fin is based upon morphological observations that usually the first two rays at the leading edge are strongly connected and create a stiffer element (Westneat et al., 2004).

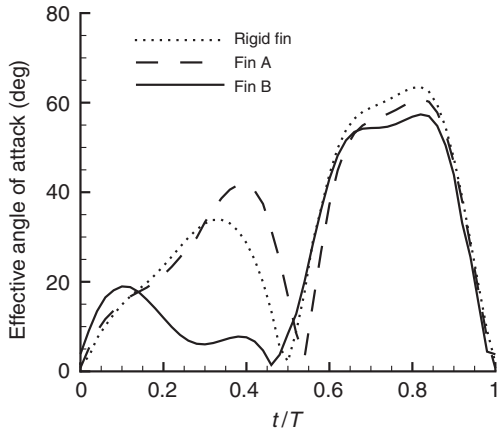

Fig. 10. Variations of the effective angle of attack at the leading edge over one period. St=0.4, Ψ_{12}=60 deg.

In Fig. 6, we plot the time history of the thrust force, the lift force, the lateral force and the power expenditure over one motion period for a fin with rigid rays and the aforementioned flexible fins. Herein, we choose St~0.4, Ψ_{12}=60 deg, and for the flexible fins the stiffness of the rays is EI'=0.5 (except for the leading edge ray in fin B). It is seen that the effect of structural flexibility is most pronounced during the first half period, i.e. the recovery stroke. What is interesting is that the fins with and without reinforcement at the leading edge display completely different behaviors. As shown in Fig. 6A, in comparison with the fin with rigid rays, with Ray 1 strengthened fin B leads to an (albeit not significant) increase in C_T. Fin A, on the other hand, generates a smaller C_T than the fin with rigid rays, especially near the end of the recovery stroke when it produces negative thrust. During the recovery stroke, compared with the fin with rigid rays, fin A also creates larger forces in the vertical direction (Fig. 6C) and the lateral direction (Fig. 6B). By contrast, Fin B reduces both C_T and C_y, although the changes are slight (just like the changes in C_T) in comparison with the fin with rigid rays. In terms of power expenditure (Fig. 6D), a large increase and decrease are observed in fin A and fin B, respectively. Most of the change occurs during the recovery stroke. This, together with the data in Fig. 6A,

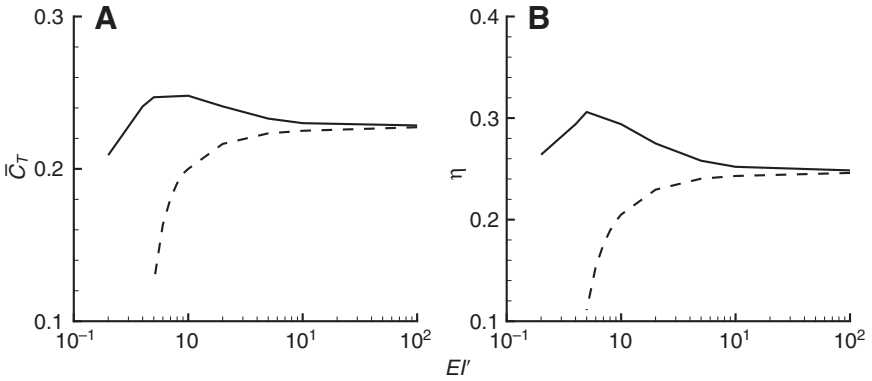

Fig. 11. (A) The mean thrust coefficient ($\bar{C}_T$) and (B) the propulsion efficiency (η) as functions of normalized bending stiffness (EI') for fin A (broken lines) and fin B (solid lines). St=0.4, Ψ_{12}=60 deg.

suggests significant efficiency enhancement by fin B and decrease by fin A. Indeed, for the particular case shown in Fig. 6, the propulsion efficiencies of the fin with rigid rays, fin A and fin B are 0.25, 0.11 and 0.30, respectively.

We also note that in all the cases shown in Fig. 6, positive thrust is generated in both the power stroke (adduction) and most of the recovery stroke (abduction) (although the thrust generated during the recovery stroke is much smaller than that during the power stroke). Besides, during the recovery stroke the fin generates a large lift force. Both of these characteristics, and even the values of C_T and C_L, are consistent with measurements of species such as bird wrasse, a fish utilizing mostly flapping fin motions [see, for example, fig. 3 in Walker and Westneat (Walker and Westneat, 2002a)]. On the other hand, by applying a smaller flapping angle ϕ_0 (e.g. ϕ_0=75 deg), it is observed that during the recovery stroke the fin generates mostly negative thrust force, resembling the behavior of the threespine stickleback, a fish using mostly rowing fin motions.

To understand the fluid–structure interaction mechanism that contributes to the aforementioned performance change by ray flexibility, in Fig. 7 we plot snapshots of the fin deformations during one motion period for the fin with rigid rays, fin A and fin B. The primary difference in the fin shape occurs near the leading edge of the fins as they undergo flapping/rowing motions within the recovery stroke (for example, see the snapshots at t=3T/8). In fin A, the leading edge bends slightly upwards against the direction of the downward flapping motion. This is attributed to the fact that the rays near the leading edge are the longest and thus least rigid. By strengthening Ray 1, it is found that the leading edge bends downwards towards the direction of flapping. This is expected to reduce the effective angle of attack at the leading edge. To illustrate this, in Figs 8 and 9 we plot the deformation of the fin together with the in-plane streamlines of the incoming flow measured in a reference system undergoing translational motions following the motion of the center point of the leading edge. The flow velocity is projected to a plane which at t=0 is parallel to the x–y plane and then rotates following the flapping motion of the fin. The reduction of the effective angle of attack in fin B is demonstrated at both t/T=π/4 and t/T=3π/8. This effect is more clearly shown in Fig. 10, where the time histories of the effective angle of attack at the center of the leading edge are shown.

To understand the performance of the flexible fins at different ray stiffness, in Fig. 11 we plot the mean $\bar{C}_T$ and the propulsion efficiency η as functions of the normalized ray stiffness EI'. The Strouhal number and the phase lag are kept unchanged. It is seen that for fin A, the more flexible the rays are, the worse the performance in thrust generation is. For fin B, on the other hand, performance enhancement is observed over the whole range of EI' considered (EI'>0.2). Maximum $\bar{C}_T$ and η occur near EI'~0.5.

In addition to the increase in thrust generation and propulsion efficiency, the structural flexibility *via* fin B also reduces the dependence upon Ψ_{12}, which measures the phase difference between the rays. As shown in Fig. 12, with fin B the curves of $\bar{C}_T$ *versus* Ψ_{12} and η *versus* Ψ_{12} are much flatter than those with the fin with rigid rays. On the other hand, no such effect is observed on the dependence upon the Strouhal number (Fig. 13).

This reduced sensitivity on kinematic parameters through structural flexibility reminds us of a similar feature of a caudal fin reinforced by flexible rays (Zhu and Shoele, 2008). In both cases, the flexible fin delivers decent performance even if the kinematic parameters are not optimized. For a fish, this greatly lowers the requirement upon accurate control of all the rays. This characteristic is also expected to be useful in biomimetic applications.

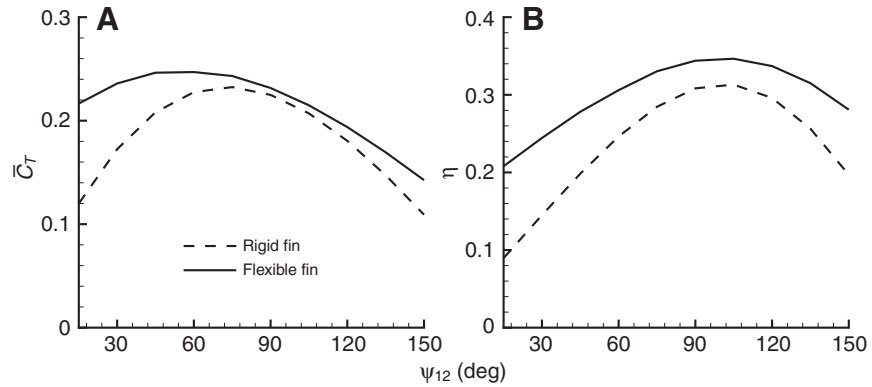

Fig. 12. (A) The mean thrust coefficient ($\bar{C}_T$) and (B) the propulsion efficiency (η) as functions of Ψ_{12} for the fin with rigid rays (broken lines) and a flexible fin (fin B) (solid lines). St=0.4, for the flexible fin EI'=0.5.

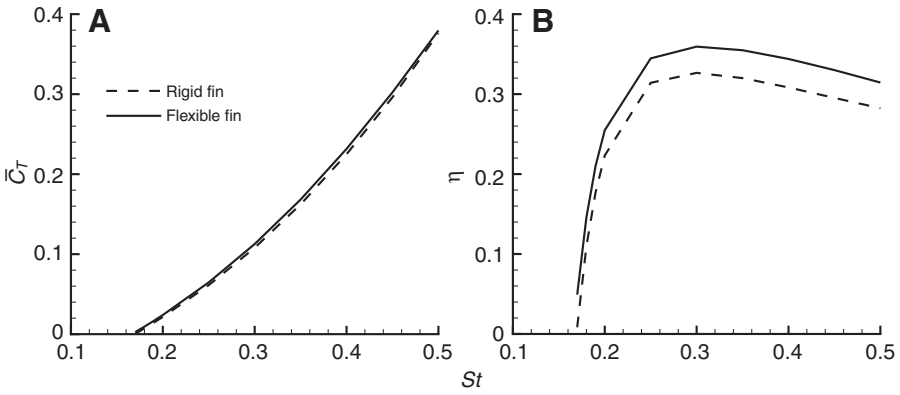

Fig. 13. (A) The mean thrust coefficient ($\bar{C}_T$) and (B) the propulsion efficiency (η) as functions of Strouhal number (*St*) for the fin with rigid rays (broken lines) and a flexible fin (fin B) (solid lines). Ψ_{12}=60 deg, for the flexible fin EI'=0.5.

Sequence of vortex shedding and near-body flow field

In order to correlate the force generation with the shedding of vortices and the induced flow in the wake, in Fig. 14 we plot snapshots of the near-body flow field at four different instants during one period. In this particular case, the rays are rigid. No significant difference is found between the wakes behind fins with rigid and flexible rays (fin A and fin B). Two of these snapshots are within the recovery stroke (t=T/4 and t=T/2), the other two (t=3T/4 and t=T) are within the power stroke. This figure displays the in-plane streamlines within the same plane that was used to depict the flow near the leading edge (ref. Figs 8 and 9), although herein the flow velocity is measured in a space-fixed reference system. This plane is defined in the following way: at the beginning of the period, this plane intersects the leading edge at its center, and it is also parallel to the x–y plane; for the rest of the period, this plane remains parallel to the x-axis and attached to the center of the leading edge; however, it follows the flapping motion of the fin so that it rotates with respect to the x-axis.

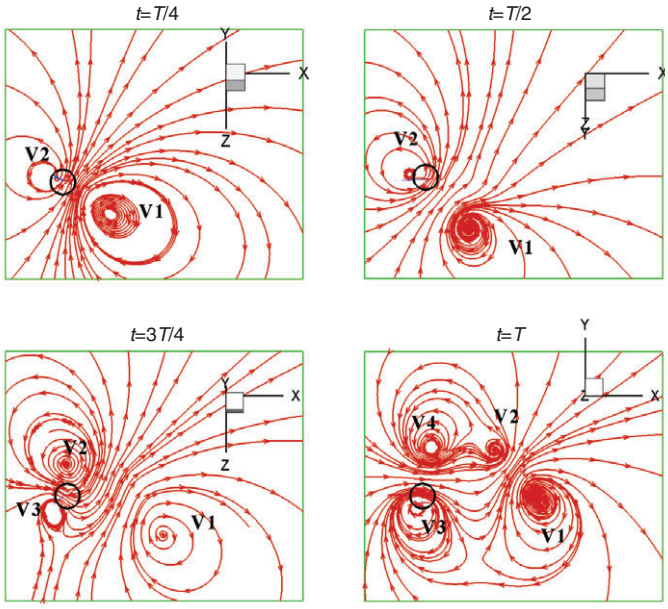

Fig. 14. Sequence of in-plane streamlines near the fin during one period of motion. The location of the fin is illustrated by the black circle. The translational motion is from right to left. The plane is located at the center of the leading edge and it rotates following the flapping motion of the fin. *St*=0.4, Ψ_{12}=60 deg.

As illustrated in Fig. 14, during the recovery stroke, a pair of counter-rotating vortices (V1 and V2) is generated. Between these two vortices, a jet flow is induced. This jet forms a large angle with the x-axis, explaining the characteristic shown in Fig. 6 that during the recovery stroke the fin produces large lift (Fig. 6C) and lateral (Fig. 6B) forces but small thrust force (Fig. 6A). During the power stroke, two more vortices (V3 and V4) are created. The jet flow induced by these two, on the other hand, is better aligned with the x-axis so that a large thrust force and a smaller lift force are generated during the power stroke.

Conclusions

By using a fully coupled fluid–structure interaction model, we numerically studied the dynamics of an idealized pectoral fin that includes a soft membrane reinforced by embedded beams representing fin rays. During the locomotion, a back-and-forth rowing motion and an up-and-down flapping motion are activated through rotations of the rays as well as pitching of the baseline. Passive fin deformations determined by the bending of the rays are considered.

Through numerical simulations we have illustrated effects of kinematic parameters and structural properties of rays upon the performance of the fin in force generation. The key kinematic factors are the frequency of motion (represented by the Strouhal number), the phase lag between rays, and the pitching motion of the baseline. Among these, the pitching motion of the baseline is found to increase the thrust force and the propulsion efficiency. It is thus an important mechanism enhancing the locomotion performance of the fish in straightline swimming.

One of the most important findings of our numerical simulation is the subtlety of the effect of structural deformability upon the performance of the fin. Two slightly different fins, one with strengthened leading-edge ray and the other without, display completely different mechanical behaviors. In fact, without leading-edge ray strengthening, the propulsion performance is greatly compromised in comparison with fins with rigid rays. The underlying physical mechanism involves the reduction of the effective angle of attack at the leading edge, which diminishes power expenditure during the recovery stroke. More generally, this observation shows that the performance of the fin is affected by spatial distribution of stiffness among the rays, as happens in real cases where mechanical properties of rays may vary across the fin.

The time history of force generation is also studied. During the recovery stroke, the fin generates a relatively small (if not negative) thrust force, the lateral force generations during the recovery and the power strokes are comparable with each other, and the lift force generated during the recovery stroke is larger than that created during the power stroke. This feature is correlated with the near-body flow field. A pair of vortices is created in the recovery stroke. The induced jet flow between them orients away from the direction of propulsion. On the other hand, the jet flow induced by another pair of vortices shed during the power stroke is better aligned with the direction of swimming.

LIST OF SYMBOLS

C_L	lift coefficient
$C_T(\bar{C}_T)$	(mean) thrust coefficient
C_y	lateral force coefficient
d	thickness of the fin
E	Young's modulus of the rays
EI'	normalized bending stiffness
$\mathbf{F}$	hydrodynamic force
$F_T(\bar{F}_T)$	(mean) thrust force
L	length of Ray 1 (the leading-edge ray)
p	hydrodynamic pressure
$P(\bar{P})$	(mean) power spent
S_b	surface of the fin
St	Strouhal number
t	time
T	$2\pi/\omega$ period of motion
T_p	duration of the power stroke
T_r	duration of the recovery stroke
U	forward speed
$\mathbf{V}_b$	velocity of the body
$\mathbf{x}=(x, y, z)$	global coordinate system
α_0	maximum angle of rolling of each ray in one stroke
α_i	angle between the i-th ray and the x-axis
α_{i0}	angle between the i-th ray and the x-axis at the initial state
η	propulsion efficiency
θ_b	pitching angle of the baseline
ν	material damping coefficient of the rays
ρ	density of fluid
ϕ_i	rotation of the i-th ray around the x-axis
Φ	flow potential
ψ_i	phase of the i-th ray in rolling

ACKNOWLEDGEMENTS

This study was supported by the National Science Foundation under grant CBET-0844857. Computational supports from TeraGrid resources provided by the San Diego Supercomputer Center and the National Center for Supercomputing Applications are acknowledged.

REFERENCES

Alben, S., Madden, P. G. and Lauder, G. V. (2007). The mechanics of active fin-shape control in ray-finned fishes. *J. R. Soc. Interface* **4**, 243-256.
Blake, R. W. (1977). On ostraciiform locomotion. *J. Mar. Biol. Assoc. UK* **57**, 1047-1055.
Blake, R. W. (1979). The mechanics of labriform locomotion. I. Labriform locomotion in the angelfish (*Pterophyllum eimekei*): an analysis of the power stroke. *J. Exp. Biol.* **82**, 255-271.
Blake, R. W. (1983). *Fish Locomotion*. Cambridge, UK: Cambridge University Press.
Bozkurttas, M., Mittal, R., Dong, H., Lauder, G. V. and Madden, P. (2009). Low dimensional models and performance scaling of a highly deformable fish pectoral fin. *J. Fluid Mech.* **631**, 311-342.
Drucker, E. G. and Lauder, G. V. (2003). Function of pectoral fins in rainbow trout: behavioral repertoire and hydrodynamic forces, *J. Exp. Biol.* **206**, 813-826.
Drucker, E. G., Walker, J. A. and Westneat, M. W. (2006). Mechanics of pectoral fin swimming in fishes. In *Fish Biomechanics*, Vol. 23 (ed. R. E. Shadwick and G. V. Lauder), pp. 369-423. San Diego, CA: Elsevier Academic Press.
Gibb, A. C., Jayne, B. C. and Lauder, G. V. (1994). Kinematics of pectoral fin locomotion in the bluegill sunfish *Lepomis macrochirus*. *J. Exp. Biol.* **189**, 133-161.
Harder, W. (1975). *Anatomy of Fishes*. Stuttgart: E. Schweizerbart'sche Verlagsbuchhandlung.
Kardong, K. V. (1998). *Vertebrates: Comparative Anatomy, Function, Evolution*, 2nd edn. Dubuque: W. C. Brown.
Lauder, G. V. and Jayne, B. C. (1996). Pectoral fin locomotion in fishes: testing drag-based models using three-dimensional kinematics. *Am. Zool.* **36**, 567-581.
Lauder, G. V. and Madden, P. G. A. (2007). Fish locomotion: kinematics and hydrodynamics of flexible foil-like fins. *Exp. Fluids* **43**, 641-653.
Lauder, G. V., Madden, P. G. A., Mittal, R., Dong, H. and Bozkurttas, M. (2006). Locomotion with flexible propulsors: I. Experimental analysis of pectoral fin swimming in sunfish. *Bioinspir. Biomim.* **1**, S25-S34.
Mittal, R., Dong, H., Bozkurttas, M., Lauder, G. V. and Madden, P. (2006). Locomotion with flexible propulsors: II. Computational modeling of pectoral fin swimming in sunfish. *Bioinspir. Biomim.* **1**, 35-41.
Shoele, K. and Zhu, Q. (2009). Fluid-structure interactions of skeleton-reinforced fins: performance analysis of a paired Fin in lift-based propulsion. *J. Exp. Biol.* **212**, 2679-2690.
Standen, E. M. (2008). Pelvic fin locomotor function in fishes: three-dimensional kinematics in rainbow trout (*Oncorhynchus mykiss*). *J. Exp. Biol.* **211**, 2931-2942.
Tjavaras, A. A., Zhu, Q., Liu, Y., Triantafyllou, M. S. and Yue, D. K. P. (1998). The mechanics of highly-extensible cables. *J. Sound Vibration* **213**, 709-737.
Videler, J. J. (1993). *Fish Swimming*. London: Chapman and Hall.
Vogel, S. (1994). *Life in Moving Fluids. The Physical Biology of Flow,* 2nd edn. Princeton, NJ: Princeton University Press.
Walker, J. A. (2004). Dynamics of pectoral fin rowing in a fish with an extreme rowing stroke: the threespine stickleback (*Gasterosteus aculeatus*). *J. Exp. Biol.* **207**, 1925-1939.
Walker, J. A. and Westneat, M. (1997). Labriform propulsion in fishes, kinematics of flapping aquatic flight in the bird wrasse *Gomphosus varius* (labridae). *J. Exp. Biol.* **200**, 1549-1569.
Walker, J. A. and Westneat, M. W. (2002a). Kinematics, dynamics, and energetics of rowing and flapping propulsion in fishes. *Integr. Comp. Biol.* **42**, 1032-1043.
Walker, J. A. and Westneat, M. W. (2002b). Performance limits of labriform propulsion and correlates with fin shape and motion. *J. Exp. Biol.* **205**, 177-187.
Webb, P. W. (1973). Kinematics of pectoral fin propulsion in *Cymatogaster aggregata*. *J. Exp. Biol.* **59**, 697-710.
Webb, P. W. (1994). The biology of fish swimming. In *Mechanics and Physiology of Animal Swimming* (ed. L. Maddock, Q. Bone and J. M. V. Rayner), pp. 45-62. Cambridge, UK: Cambridge University Press.
Westneat, M., Thorsen, D. H., Walker, J. A. and Hale, M. (2004). Structure, function, and neural control of pectoral fins in fishes. *IEEE J. Oceanic Eng.* **29**, 674-683.
Zhu, Q. and Shoele, K. (2008). Propulsion performance of a skeleton-strengthened fin. *J. Exp. Biol.* **211**, 2087-2100.